

# Electromagnetic Source Imaging via a Data-Synthesis-Based Denoising Autoencoder

Gexin Huang, Zhu Liang Yu\*, *Member, IEEE*, Ke Liu, Zheng Hui Gu, *Member, IEEE*, Feifei Qi, Yuanqing Li, *Fellow, IEEE*, Jiawen Liang, and Wei Wu\*, *Senior Member, IEEE*,

**Abstract**—Electromagnetic source imaging (ESI) requires solving a highly ill-posed inverse problem. To seek a unique solution, traditional ESI methods impose various forms of priors that may not accurately reflect the actual source properties, which may hinder their broad applications. To overcome this limitation, in this paper a novel data-synthesized spatio-temporal denoising autoencoder method termed DST-DAE is proposed for ESI. DST-DAE recasts ESI as a machine learning problem, where discriminative learning and latent-space representations are integrated in a denoising autoencoder (DAE) to learn a robust mapping from the measured electroencephalography/magnetoencephalography (E/MEG) signals to the brain activity. In particular, by incorporating prior knowledge regarding dynamical brain activities, a novel data synthesis strategy is devised to generate large-scale samples for effectively training the DAE. This stands in contrast to traditional ESI methods where the prior information is often enforced via constraints primarily aimed for mathematical convenience. Extensive numerical experiments as well as analysis of a real MEG dataset demonstrate that DST-DAE outperforms several state-of-the-art ESI methods in robustly estimating source signals under a variety of source configurations.

**Index Terms**—electromagnetic source imaging (ESI), data synthesis, deep learning, denoising autoencoder (DAE)

## I. INTRODUCTION

The forward problem of electroencephalography/magnetoencephalography (E/MEG) involves determining the external surface potentials or magnetic fields from a given configuration of neuronal current activities. In contrast, reconstructing sources of brain activities from the external measurements of electromagnetic signals is defined as the E/MEG inverse problem, also known as the electromagnetic source imaging (ESI) problem. The solution to the ESI problem provides comprehensive spatial-temporal patterns of brain activities associated with a multitude of functions, leading to broad applications in the diagnosis and prediction of brain diseases [1]–[3]. However, due to the limited number of channels for the external measurements compared to the number of unidentified sources, the ESI problem is highly ill-posed, i.e., there are infinite possible solutions for a

given measured E/MEG signal, which poses a long-standing challenge for ESI.

To enable a unique solution, previous studies were centered on the optimization or probabilistic framework where regularization techniques or pieces of prior information are exploited to constrain the solution space. Minimum norm estimate (MNE) [4] employs the  $L_2$ -norm regularization to estimate spatially smooth sources. Its variant, weighted MNE (wMNE) [5], assigns additional weights to the sources to mitigate the bias towards superficial sources. Low-resolution electromagnetic tomography (LORETA) [6] is an alternative  $L_2$ -norm-based approach that utilizes the Laplace matrix to spatially regularize the solution. Although these methods may be suitable for imaging spatially extended sources, the  $L_2$ -norm regularization may lead to overly diffuse estimates for focal sources [7], [8]. To overcome this limitation, focal under-determined system solution (FOCUSS) [9] and sparse source imaging (SSI) [10] introduce  $L_p$ -norm regularizers that encourage sparsity of the solution. Along this line, the  $L_p$  norm iterative sparse solution (LPISS) [11] is an iterative sparse learning algorithm based on a  $L_p$  norm. Sparse Bayesian learning approaches (SBL) [12]–[14] cast the inverse problem under an empirical Bayesian framework where hyperparameters can be automatically determined and sparse solutions can be obtained. In particular, Champagne [15], [16] is an SBL approach that estimates the number, location, and time course of the sources in a principled fashion. Nevertheless, these sparse approaches are fundamentally limited in recovering the spatial extents for extended sources and may suffer from discontinuity in the reconstructed time courses under low signal-to-noise settings [17]. In addition to the smoothness and sparseness constraints, prior studies also explored the use of other constraints for source imaging. Spatiotemporal tomographic nonnegative independent component analysis (STTONNICA) [18] decomposes source signals into temporal and spatial components via nonnegative matrix factorization. In contrast, methods such as [19]–[21] exploit the physical properties of neural activity, information about the cortical tissue structures, or other modalities with high spatial resolutions such as Magnetic Resonance Imaging (MRI) to obtain more accurate source imaging results.

The aforementioned approaches attempt to solve the inverse problem in a direct manner that use varying forms of prior assumptions to constrain the solution space of the optimization problem. From a machine learning perspective, since there is no labeled data involved to train the underlying models, these approaches can also be viewed as unsupervised learning meth-

This work was supported in part by the National Natural Science Foundation of China under Grants 61836003, 61906048, and 61703065.

Z. L. Yu, Z. Gu, Y. Li, and J. Liang are with the School of Automation Science and Engineering, South China University of Technology, Guangzhou, China, 510641. Wei. Wu is with the Department of Psychiatry and Behavioral Sciences, Stanford University, Stanford, CA, USA. K. Liu is with Chongqing Key Laboratory of Computational Intelligence, Chongqing University of Posts and Telecommunications, Chongqing, 400065, China. F. Qi is with School of Internet Finance and Information Engineering, Guangdong University of Finance, Guangzhou, 510521, China (\* Corresponding author: Wei Wu. E-mail: weiwunewu@gmail.com, Zhu Liang Yu. E-mail: zlyu@scut.edu.cn)

ods. However, prior information regarding source signals is enforced via constraints often adopted to enable mathematical tractability yet may not accurately reflect the actual source configurations. Moreover, computational complexity may be increased considerably with more accurate modeling analysis [22]. For the purpose of learning the mapping from the sensor to the source space, some prior studies employed artificial neural networks to solve the dipole fitting problem [23]–[26], which assumes a small number of dipole sources are activated. Nonetheless, the problem is tractable only for one or two dipoles due to the difficulty of optimizing the neural network with more dipoles. Thanks to the rapid development of deep learning in recent years [27], deep neural networks are now capable of learning sophisticated mappings through large-scale training sets for distributed ESI, in which the mappings are represented by stacked nonlinear layers. Thus, deep neural networks may serve as a potential new solution for the ESI problem. Recently, the source imaging framework network (SIFNet) [28] was proposed in an attempt to convert the ESI inverse problem to a multi-classification problem, which falls in the realm of supervised learning. Specifically, after modeling the source space as a series of interconnected regions, a residual-block-based classification network can be successfully trained via the generated training set, where a binary training label is determined at each region to indicate its state (active or inactive). As such, SIFNet is not able to yield estimates of source time series, which nonetheless may provide critical information in many basic or translational studies.

In this paper, we propose a novel data-synthesized spatio-temporal denoising autoencoder (DST-DAE) method that reformulates the ESI problem as a machine learning problem, where discriminative learning and latent-space representations are integrated in a denoising autoencoder [29] to learn a robust mapping from E/MEG signals to sources. Notably, by incorporating the spatio-temporal properties of dynamical brain activities, a data synthesis strategy is devised to generate large-scale training samples for effectively training the DAE, where no complicated mathematical modeling of prior information is required as in the traditional framework. In addition, the structure of the DAE is tailored to E/MEG signals in that there are dedicated layers performing spatio-temporal filtering of E/MEG signals, ensuring that the spatio-temporal patterns of E/MEG signals are sufficiently leveraged to enhance the performance.

Compared to SIFNet which focuses on classifying the activation state of each brain region, DST-DAE is able to not only locate the region of brain activity but also effectively reconstruct their time courses. Furthermore, the denoising layer in DAE renders DST-DAE robust to the noise in the E/MEG signals. Experimental results show that the network can recover the spatial extents and the time courses of the sources under even low signal-to-noise settings, outperforming existing ESI algorithms.

The remainder of the paper is organized as follows. The proposed DST-DAE approach is introduced in Section II. Section III presents the experimental results on simulated and real datasets. Discussions about the merits and limitations of DST-DAE are presented in Section IV. Finally, conclusions

are provided in Section V.

## II. METHODOLOGY

### A. Problem Formulation

The forward model of the E/MEG signals can be represented as

$$\mathbf{X} = \mathbf{L}\mathbf{S} + \boldsymbol{\varepsilon}, \quad (1)$$

where  $\mathbf{X} = [\mathbf{x}_1, \dots, \mathbf{x}_t, \dots, \mathbf{x}_T] \in \mathbb{R}^{N_c \times T}$  denotes the measured E/MEG signals of  $N_c$  channels at  $T$  time points. Each column  $\mathbf{x}_t = [x_{1t}, \dots, x_{N_c t}]^T$  represents a snapshot of the signal vector at time  $t$ .  $\mathbf{S} = [\mathbf{s}_1, \dots, \mathbf{s}_t, \dots, \mathbf{s}_T] \in \mathbb{R}^{N_s \times T}$  denotes the source signals. Each column  $\mathbf{s}_t = [s_{1t}, \dots, s_{N_s t}]^T$  represents the source signal vector at time  $t$ .  $\boldsymbol{\varepsilon} \in \mathbb{R}^{N_c \times T}$  denotes the measurement noise.  $\mathbf{L}$  is the lead field matrix, which encodes how each unit source at a certain location is related to the measured E/MEG signals. The lead field matrix can typically be obtained by modeling tissues of the human head via numerical methods such as the finite element model (FEM) [30] or boundary element model (BEM) [31], based on structural MRI scans of individual subjects or an average template.

Assuming the lead field matrix  $\mathbf{L}$  has been obtained by solving the forward problem, the ESI problem aims to find a mapping  $P(\cdot)$  from E/MEG signals  $\mathbf{X}$  to source signals  $\mathbf{S}$ :

$$\mathbf{X} \xrightarrow{P(\cdot)} \mathbf{S}. \quad (2)$$

Due to the ill-posedness of the ESI problem when  $N_s \gg N_c$ , traditional methods introduce regularization techniques in order to obtain a unique solution  $\mathbf{S}^*$ . This can be typically performed explicitly by adding a regularization term to the loss function under the optimization framework or implicitly via priors in probabilistic modeling, both leading to the following solution:

$$\mathbf{S}^* = \arg \min_{\mathbf{S}} D(\mathbf{S}) + R(\mathbf{S}), \quad (3)$$

where  $D(\mathbf{S})$  measures the discrepancy between the actual and the reconstructed sensor signals based on the estimated source signals, e.g.,  $D(\mathbf{S}) = \|\mathbf{X} - \mathbf{L}\mathbf{S}\|_F^2$  [4], [5], where  $\|\cdot\|_F$  denotes the Frobenius norm.  $R(\mathbf{S})$  is the regularization term based on the estimated source signals. For instance,  $R(\mathbf{S})$  can be employed to promote the sparsity ( $L_1$  norm) or minimize the overall energy ( $L_2$  norm) of the source signals [19].

To overcome the limitation that  $R(\mathbf{S})$  is often devised for mathematical convenience yet may not accurately reflect the actual source configurations, in this paper we propose a novel deep learning approach based on a data synthesis strategy.

### B. Data-Synthesized Deep Learning Strategy

DST-DAE views the ill-posed inverse problem as a multi-target regression problem that aims to uncover the mapping  $P_\theta(\cdot)$  via a nonlinear neural network, where  $\theta$  represents the unknown weights of the neural network. In order to render the neural network approach feasible, sufficient source and E/MEG data samples should be provided for training the neural network. However, in vivo source data samples are

hardly acquired in practice as direct recordings of electrical brain activities are invasive. In this paper, to better reflect the spatio-temporal properties of the source signals, we inject prior information regarding the temporal realistic activities and the spatial compactness into data synthesis. These properties encoded in the synthesized data can then be effectively learned by training the neural network, of which the specific architecture is illustrated in Section II-C.

The proposed DST-DAE is depicted in Fig. 1. Specifically, the data synthesis strategy is based on the realistic forward model derived from anatomical MRI scans and temporal basis functions derived from realistic scalp signals. First, the source data are decomposed into temporal and spatial components where various spatial and temporal states are generated by uniformly sampling from the respective prior space (Details are provided in section II-D). Second, the generated source signals, denoted as  $S_g$ , are obtained via the product of the temporal signals and the source active states, and the corresponding E/MEG signals, denoted as  $X_g$ , can be simulated by passing  $S_g$  through the forward model. As such, a large-scale dataset of source and E/MEG signals with varying states can be generated as the training set to learn  $P_\theta(\cdot)$ . Under the loss function  $\mathcal{L}_\theta(\cdot)$ , the optimal parameters can be obtained as  $\theta^* = \arg \min_\theta \mathcal{L}_\theta(X_g, S_g)$  based on the training set. Finally, the learned inverse mapping  $P_{\theta^*}(\cdot)$  can be used for ESI on unseen E/MEG signals. The implementation details are provided in Section II-D.

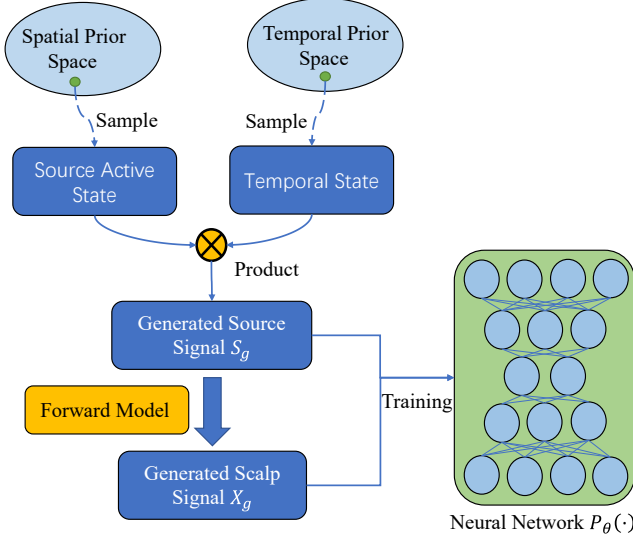


Fig. 1: Data-synthesized deep learning strategy for solving the ESI problem.

### C. Neural Network Design

As opposed to taking a pure discriminative approach to solving the multi-target regression problem, which may be prone to overfitting in the presence of noise in the E/MEG signals, we propose a more robust approach that integrates discriminative learning and latent-space representation under the framework of the DAE. Inspired by the EEG decoding

network [32]–[34], through blocks with spatio-temporal step-wise convolution/deconvolution tailored to E/MEG signals, the latent-space representation in the DAE is capable of extracting robust features from noisy E/MEG signals that capture the underlying dependencies and spatio-temporal structure, hence effectively regularizing the solution when combined with discriminative learning.

1) *Architecture*: The overall network structure is shown in Fig. 2(a). The generated E/MEG signals  $X_g$  and the corresponding generated source signals  $S_g$  are fed into the neural network as training samples, and  $X_n$  is the noise corrupted version of  $X_g$ . The encoder contains a noise layer and two feature extraction blocks: temporal and spatial encoding blocks. Specifically, through the temporal encoding block, the temporal feature  $X_t$  is extracted from the noise corrupted E/MEG signals afforded by the noise layer. The spatial block then generates the spatio-temporal feature  $X_{st}$ . In the decoder, which consists of spatial and temporal decoding blocks and a forward transformation layer, the spatial decoding block first decodes spatial information from  $X_{st}$ , yielding the source temporal features  $S_t$ . The temporal block then computes the reconstructed source signal  $S_{re}$  by decoding the temporal information. Finally, the forward transformation layer calculates the reconstructed scalp signal  $X_{re}$  as the output of the DAE. Unlike in the traditional DAE, here the loss function is the weighted sum of the discrepancy between  $S_{re}$  and  $S_g$  and the discrepancy of  $X_{re}$  and  $X_g$ . The former measures the error between the predicted and true response variables from the perspective of multi-target regression, hence falling under the umbrella of discriminative learning. The latter aligns with the loss function in the traditional DAE, which measures the adequacy of the DAE for latent-space representation.

2) *Encoder and Decoder*: The details of the neural network are illustrated in Fig. 2(b). The network is comprised of 6 layers:

**Noise block**  $\mathfrak{N} (\mathbb{R}^{N_c \times T} \rightarrow \mathbb{R}^{N_c \times T})$ : This block yields  $X_n$  by corrupting  $X_g$  with white Gaussian noise with a specific SNR. Note this block is only used during the training period.

**Temporal encoding block**  $\mathfrak{h} (\mathbb{R}^{N_c \times T} \rightarrow \mathbb{R}^{N_c \times K_t \times F_1})$ : This block contains multiple stacks of 2-D convolution layers with a convolution kernel of  $1 \times 5$  and a step size of  $1 \times 2$ , where a convolution layer with the same kernel size but a  $1 \times 1$  step size is added after each layer to enhance the modeling capability. The kernel size allows the block to perform temporal convolution separately for each channel of E/MEG signals, thus extracting the temporal features  $X_t = \mathfrak{h}(X_n)$  that contains  $F_1$  temporal feature maps with a temporal size of  $K_t$ .

**Spatial encoding block**  $\mathfrak{g} (\mathbb{R}^{N_c \times K_t \times F_1} \rightarrow \mathbb{R}^{1 \times K_t \times K_s})$ : This block contains a 2-D convolution layer with a convolution kernel of  $N_c \times 1$  and a step size of  $1 \times 1$ . Therefore, it performs a full-channel spatial convolution at each time point and extracts the spatio-temporal feature maps  $X_{st} = \mathfrak{g}(X_t)$  with a size of  $K_s \times K_t$ .

**Spatial decoding block**  $\mathfrak{g}^{-1} (\mathbb{R}^{1 \times K_t \times K_s} \rightarrow \mathbb{R}^{N_s \times K_t \times F_2})$ : This block contains multiple stacks of 2-D deconvolution layers with a kernel size of  $10 \times 1$  and a step size of  $2 \times 1$ . It decodes spatial information from  $X_{st}$  to yield the

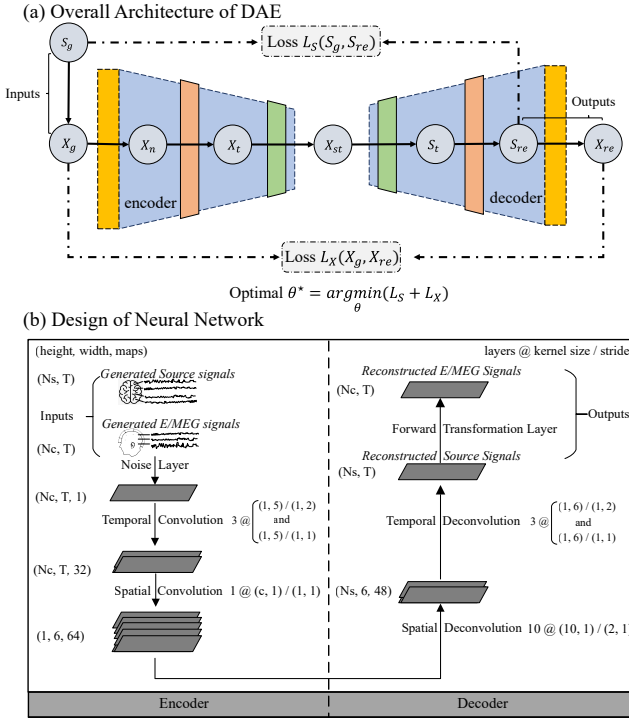


Fig. 2: Overall architecture and design of the DAE. (a) Overall architecture. The arrows indicate the input-to-output sequence of the DAE, and the dashed lines indicate the connected tensors to calculate the corresponding loss function. (b) Detailed design of the neural network.  $N_c$  and  $N_s$  represent the number of sensors and sources, respectively.  $T$  is the total number of time points. In our experiments, we downsampled the time points to 40.

source temporal features  $S_t = g^{-1}(X_{st})$  that contains  $F_2$  deconvolution feature maps with a size of  $N_s \times K_t$ .

**Temporal decoding block**  $h^{-1}(\mathbb{R}^{N_s \times K_t \times F_2} \rightarrow \mathbb{R}^{N_s \times T})$ : This block contains multiple 2-D deconvolution layers with a kernel size of  $1 \times 6$  and a step size of  $1 \times 2$ , where a deconvolution layer with the same kernel size but a  $1 \times 1$  step size is also added after each layer. We set the kernel size of the deconvolution layer to an even number (i.e., 6) to avoid checkerboard artifacts [35]. This block further decodes  $S_t$  to estimate the reconstructed source signals  $S_{re} = h^{-1}(S_t)$ .

**Forward transformation block**  $f(\mathbb{R}^{N_s \times T} \rightarrow \mathbb{R}^{N_c \times T})$ : This block calculates the reconstructed E/MEG signals through the lead field matrix:  $X_{re} = L S_{re}$ .

To accelerate network training, the exponential linear unit (*elu*) function [36] is employed as the activation function for all convolution and deconvolution layers except the last deconvolution layer preceding  $S_t$ , which uses the linear activation function instead. Furthermore, as suggested in [37], a Batch Normalization (BN) layer is added between the convolution/deconvolution layer and the activation layer. This overcomes the distribution shift and the covariate drift that may occur during feature transformation especially in training with a large-scale dataset, preventing loss oscillation, weight saturation, and decelerated learning. According to our experi-

ments, with the BN layer introduced in the neural network, the solution is not only insensitive to the parameter initialization in each layer but also able to converge quickly and smoothly.

3) *Loss Function*: In this paper, two error functions quantifying the reconstruction error for the source signals and that of the E/MEG signals are proposed. The loss function is the weighted sum of the two error functions:

$$\mathcal{L}_{\theta}(X_g, S_g) = \lambda_1 \mathcal{L}_X(X_g, X_{re}) + \lambda_2 \mathcal{L}_S(S_g, S_{re}), \quad (4)$$

where  $\lambda_1 \geq 0$  and  $\lambda_2 \geq 0$  are the loss weights (see Supplementary Materials for further discussions), and

$$\mathcal{L}_X(X_g, X_{re}) = \frac{1}{N} \sum_i \|X_g^{(i)} - X_{re}^{(i)}\|_F^2, \quad (5)$$

$$\mathcal{L}_S(S_g, S_{re}) = \frac{1}{N} \sum_i \left[ \|S_g^{(i)} - S_{re}^{(i)}\|_F^2 + \delta \|S_g^{(i)} - S_{re}^{(i)}\|_{1,1} \right], \quad (6)$$

where  $\|\cdot\|_{1,1}$  is the  $L_{1,1}$  matrix norm defined as  $\|A\|_{1,1} = \sum_{j=1}^N \sum_{i=1}^m |a_{ij}|$ ;  $N$  is the total number of training samples and  $\delta \geq 0$  is a manually set parameter. To facilitate precise reconstruction of the sources by the network, we use the weighted sum of the mean square error (MSE) and mean absolute error (MAE) to assess the reconstruction error for the source signals, since the MSE is more sensitive to high amplitude errors while the MAE is more sensitive to subtle differences in the amplitude. However, for the E/MEG signals, due to the presence of noise in the data, excessively pursuing the reconstruction accuracy may lead to overfitting. Therefore, we use the mean square error (MSE) alone to measure the reconstruction error.

In contrast to the standard DAE that only attempts to learn a latent-space representation for E/MEG (Equation (5)), the loss function for DST-DAE additionally incorporates the optimization of the source signals as in Equation (6), which are what the ESI strives to estimate. Moreover, since the generated source signals encode our prior knowledge regarding the true dynamics of brain activities, our approach provides a convenient framework for leveraging prior information regarding source signals as long as it is properly reflected in the data synthesis step. Thus, a notable difference of our approach from traditional ESI methods is that the prior information regarding source signals is not enforced via mathematical constraints typically presented as the  $L_1$  norm or  $L_2$  norm of the source signals for mathematical convenience, which nonetheless may not accurately reflect that the actual source configurations.

Performance comparisons of different ESI algorithms are presented in Section sections III-B to III-E to demonstrate the advantages of DST-DAE.

#### D. Implementation Details

The workflow of DST-DAE consists of three phases: data synthesis phase, training phase and source estimation phase.



1) *Data Synthesis Phase*: To ensure that the training data faithfully reflect the spatio-temporal properties of realistic brain activity, the proposed data strategy incorporate spatial and temporal information of brain activity into the generation of source signals:

$$\mathbf{S}_g = \mathbf{W}\Phi = \sum_{k=1}^K \mathbf{w}_k \phi_k, \quad (7)$$

where  $\Phi \in \mathbb{R}^{K \times T}$  is the temporal state matrix and  $\mathbf{W} \in \mathbb{R}^{N_s \times K}$  represents the activation state matrix of brain sources with  $K$  spatial components.  $\phi_k$  is the  $k$ -th temporal component generated from a set of  $m$  temporal basis functions (TBFs)  $\Theta \in \mathbb{R}^{m \times T}$ .  $\mathbf{w}_k$  is the  $k$ -th spatial component:

$$\mathbf{w}_k = \begin{cases} 1 & s_j \in \gamma \\ 0 & \text{else} \end{cases}, \quad (8)$$

where  $s_j$  represents the  $j$ -th vertex of the source, and  $\gamma$  represents the index set of activated sources.

For the purpose of large-scale training, we generate training samples with varying spatial activation states  $\mathbf{W}$  and temporal states  $\Phi$  as follows. For the  $i$ -th generated sample, first, we sample from a uniform distribution to obtain the seed source  $s_{seed}$  in the source space. Subsequently, the spatial activation state is generated as a binary vector whose activated sources are indexed as 1, wherein the index set of activated sources is obtained by gradually expanding activated sources within the seed's neighborhood  $n$  until the total area is subject to a given value  $A$ :  $\gamma_k^{(i)} = \{s_j | \text{area}(\gamma) = A, s_j \in n(s_{seed})\}$ , where  $A$  is randomly sampled from a uniform distribution between 0 and  $A_{max}$ .  $A_{max}$  is set to 20 as it has been shown the area of cortex activity is typically 10–20  $\text{cm}^2$  [38]. The generated spatial states can be spatially contiguous and locally homogeneous as suggested by previous studies [39], [40].

Second, methods such as the stimulus evoked factor analysis (SEFA) [41] or singular value decomposition (SVD) [42] can be used to estimate the TBFs from realistic E/MEG signals  $\mathbf{X}_{real}$  (see Sections III-C and III-G). Then,  $\phi_k^{(i)}$  is generated from the subspace spanned by  $\Theta$  as  $\phi_k^{(i)} = \sum_{m=1}^M \zeta_m^{(i)} \Theta(m)$ , where the weight  $\zeta_m^{(i)}$  is obtained from uniform sampling.

Finally, the  $i$ -th generated source signals  $\mathbf{S}_g^{(i)}$  can be obtained as the product of the spatial activation state  $\mathbf{W}^{(i)}$  and the temporal state  $\Phi^{(i)}$ , and the corresponding E/MEG signals  $\mathbf{X}_g^{(i)}$  can be generated by passing the generated source signals through the forward model with the lead field matrix  $\mathbf{L}$  derived from solving the forward problem.

2) *Training Phase*: The generated dataset  $(\mathbf{S}_g, \mathbf{X}_g)$  is used to train the neural network, where the SNR of the E/MEG signals determines the noise level in the noise block to corrupt  $\mathbf{X}_g^{(i)}$ . Through minimizing the loss function until convergence, the trained neural network is capable of automatically learning the mapping from the E/MEG signals to the source signals.

3) *Source Estimation Phase*: In this phase, the trained neural network is applied to map unseen realistic E/MEG signals  $\mathbf{X}_{real}$  to source signals  $\mathbf{S}^*$ .

### III. EXPERIMENTS

In this section, we present experiments using simulated and realistic data to demonstrate the efficacy of DST-DAE. Specifically, four simulated experiments were devised to compare the performance of DST-DAE to that of several existing ESI methods, including two  $L_2$ -norm methods, wMNE [5] and LORETA [6], which were proposed for the reconstruction of spatially extended source, two sparse-constrained methods, SBL [15] and FOCUSS [9], which were designed for estimating focal sources, and a spatio-temporal constrained method, STTONNICA [18], which decomposes source signals into spatial and temporal components that are optimized under the Bayesian information criterion (BIC). The performance of DST-DAE is assessed by evaluating the recovered source signals under a variety of experimental settings using multiple metrics. An additional experiment was conducted to study the impact of training sample size on the performance of DST-DAE. Finally, a real MEG dataset was analyzed to further illustrate the superiority of DST-DAE in practice.

#### A. Experimental Description and Performance Metrics

1) *Protocol of Simulation Experiments*: Throughout the following experiments, the cortical surface was obtained by segmenting the white/gray matter interface of default MR images derived from MNI/ICBM152 using Brainvisa<sup>1</sup>. The cortical surface was then tessellated with triangles and the resulting cortical mesh was downsampled to a total of 1,024 triangular elements in order to build the cortex space. The sensor template was configured as the 65-channel Neuroscan Quikcap system. The lead field matrix  $\mathbf{L}$  was computed using the BEM method. This forward modeling process was implemented using the OpenMEEG plug-in [43] in Brainstorm [44].

The time course of each patch source was simulated as a Gaussian damped sinusoidal time course:  $\sin(2\pi f) \exp^{-(t-\tau)/\omega}$ . Through the choice of different  $f$ ,  $\omega$ , and  $\tau$ , event-related potential (ERP) signals with various temporal states could be simulated. A source active region was simulated by selecting a triangular element on the cortical mesh as a seed voxel in the regional center and enlarging the region by iteratively absorbing its neighbor elements until the required area condition was achieved. The source signals were constructed by placing the simulated ERP signals at the source active regions, and the corresponding EEG signals were calculated via the forward model. White Gaussian noise with a specific SNR was added to the simulated signals. The SNR was defined as  $SNR = 10 \log_{10} \frac{\|\mathbf{L}\mathbf{S}\|^2}{\|\boldsymbol{\epsilon}\|^2}$ . In our simulation experiments, we generated the ERP signal with 40 sampling points per trial, and the TBFs were obtained from the simulated E/MEG signals by SEFA. Without loss of generality, the number of TBFs was 4.

In simulation experiments, we considered four scenarios to assess the reconstruction performance of DST-DAE against aforementioned compared methods:

<sup>1</sup><http://www.brainvisa.info>.

- Single active patch source with varying SNRs: we fixed the source area at  $5 \pm 0.58 \text{ cm}^2$  and varied the SNR from -5 dB, 0 dB, 5 dB, to 10 dB.
- Single active patch source with varying spatial extents: we fixed the SNR at -5 dB and varied the source area from  $3 \text{ cm}^2$ ,  $6 \text{ cm}^2$ ,  $10 \text{ cm}^2$ , to  $15 \text{ cm}^2$ .
- Two patch sources with varying spatial patterns: we fixed the SNR at -5 dB and varied the source pattern from  $4 \text{ cm}^2$  and  $4 \text{ cm}^2$ ,  $4 \text{ cm}^2$  and  $10 \text{ cm}^2$ ,  $10 \text{ cm}^2$  and  $4 \text{ cm}^2$ , to  $10 \text{ cm}^2$  and  $10 \text{ cm}^2$ .
- Two patch sources with varying correlated sources: we fixed SNR at -5 dB and the source area at  $7 \text{ cm}^2$ . The coefficient correlation between the two patch source signals was varied from 0, 0.3, 0.6, to 0.9.

For each experimental setting, 100 Monte Carlo numerical simulations were performed to statistically evaluate the reconstruction performance.

2) *Parameter Setting*: The proposed network was coded in Python with Keras library using TensorFlow Backend. Adam, which is a gradient-based optimization algorithm, was chosen as the optimizer. The impact of the hyperparameters on the predictive performance of the neural network was systematically studied on separately generated data (see Section IV-A for details). In short, the predictive performance of the neural network favors the following settings of the key hyperparameters: 1) small kernel sizes and small strides in the temporal encoding and decoding layers; 2) large kernel sizes and small strides in the spatial encoding and decoding layers. In particular, a kernel size equal to the channel number in the spatial convolution layer is preferred; and 3) increasing numbers of feature maps for the encoder and decreasing numbers of feature maps for the decoder. These observations therefore motivated us to set the kernel size and stride as in Fig. 2. Moreover, we set  $K_t = 5$  and  $K_s = 64$  for the spatio-temporal feature  $\mathbf{X}_{st}$ . The optimal ratio of loss weights are  $\lambda_2 : \lambda_1 = 15 : 1$ . The learning rate of the Adam optimizer was set to  $10^{-4}$ , and the other hyperparameters of the Adam optimizer were set to the values suggested in [45], i.e.,  $\beta_1 = 0.9$ ,  $\beta_2 = 0.999$  and  $\epsilon = 10^{-8}$ . The batch size was set to 32 for the mini-batch stochastic gradient descent, and all the trainable parameters in the neural network were initialized with the Glorot Uniform method. The iteration number of the model training was set to 300. We used a weight decay strategy for every convolution/deconvolution layer by employing the  $L_1$  and  $L_2$  regularizers, for which the regularization penalty is  $10^{-3}$ .  $\delta$  in the loss function was set to 0.1.

To further improve the performance of DST-DAE, we utilized a warm-up strategy [46] to dynamically fine-tune the learning rate during the training. The learning rate was linearly increased to the maximum in the initial 20 epochs and linearly decreased to the minimum in the last 20 epochs.

3) *Performance Metrics*: In the simulation experiments, the performance of all the ESI methods was assessed with the following four metrics:

- Area under the receiver operating characteristic curve (AUC), which evaluates the sensitivity and specificity of the source detection.

SNR (dB)	-5	0	5	10
RMSE	$0.781 \pm 0.036$	$0.519 \pm 0.029$	$0.269 \pm 0.015$	$0.132 \pm 0.005$

TABLE I: RMSE values between simulated EEG signals and reconstructed signals. The mean and standard deviation are calculated by 100 Monte Carlo simulations per SNR.

- Relative mean square error (RMSE), which evaluates the accuracy of the reconstructed time courses.
- Distance of localization error (DLE), which measures the localization error through the average distance from the activity peak of the estimated sources to those of the true ones.
- Spatial dispersion (SD), which measures the extent to which the estimated sources are spatially blurred.

These metrics allow us to comprehensively evaluate each ESI method in terms of its ability to localize and estimate the spatial extent of the sources. In general, a desirable method is expected to achieve a relatively high AUC value and small RMSE, SD, and DLE values. Furthermore, as an indicator of the generalization performance of the trained network, we calculated the R-square ( $R^2$ ) [47] values between the estimated and true source signals in the validation set unused in the training stage. Source maps were thresholded using the Otsu's method [48]. Details of each metric and the Otsu's method are provided in Supplementary Materials.

### B. Experiment I: Single Patch Source with Varying SNRs

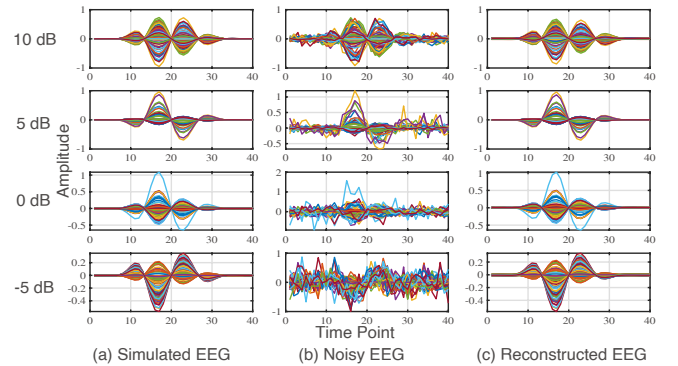


Fig. 3: Denoising performance of DAE for EEG signals with varying SNRs. The left column represents noiseless EEG signals randomly sampled from each group of test samples. The middle column represents the corresponding noisy signals. The right column represents the reconstructed signals that are denoised via the neural network.

The first experiment evaluates the reconstruction performance for source signals and EEG signals with varying SNRs when the spatial extent of the patch source is fixed at  $5 \text{ cm}^2$ . As shown in Fig. 3 and Table I, DST-DAE can accurately reconstruct the time courses of the EEG signals even with heavy noise in the data.

Fig. 4 depicts the four performance metrics over 100 Monte Carlo simulations. For the AUC value, the performance of wMNE and LORETA worsens as the noise level increases,

while STTONNICA, SBL, and FOCUSS are more robust to noise. Among all the methods, DST-DAE achieves the highest AUC value, which remains stable across all the noise levels. For the RMSE value, all the algorithms' performance declines with increasing noise. However, DST-DAE substantially outperforms the other algorithms under all the SNRs with at least 5-fold improvement. Furthermore, DST-DAE achieves low DLE and SD values as SBL and FOCUSS do. However, SBL and FOCUSS are sparse algorithms that favor focal sources at the price of higher RMSE and lower AUC values.

To illustrate, a source imaging example is presented in Fig. 5. As can be seen, the  $L_2$ -norm based methods, namely wMNE and LORETA, lead to diffuse source estimates, which aggravates as the noise increases. By contrast, the sparse methods, namely SBL and FOCUSS, tend to split patch sources into focal sources, resulting in spurious sources with increasing noise. STTONNICA yields relatively compact sources. However, the amplitude of the sources is not accurate compared to the ground truth. Since DST-DAE does not make biased assumptions regarding the sources, it can faithfully recover the spatial extent of the sources with accurate estimation of their amplitude. Therefore, both the quantitative and qualitative results demonstrate the robustness of DST-DAE compared to the other algorithms.

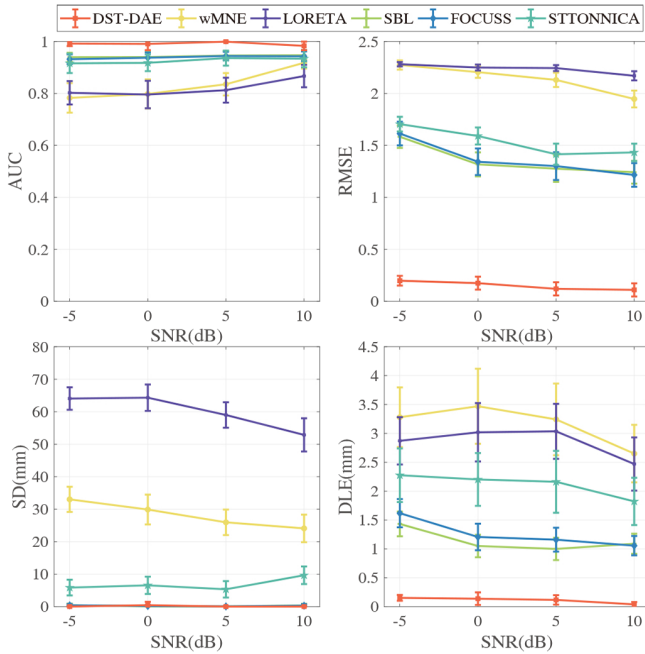


Fig. 4: Performance metrics for the single patch source with varying SNRs. Results are assessed across 100 Monte Carlo simulations and shown as mean  $\pm$  SEM (SEM: standard error of the mean). There are four metrics: 1) AUC evaluates the sensitivity and specificity of source localization, 2) RMSE evaluates the accuracy of the reconstructed time courses, 3) SD measures the spatial blurred extent, and 4) the DLE quantifies the localization error.

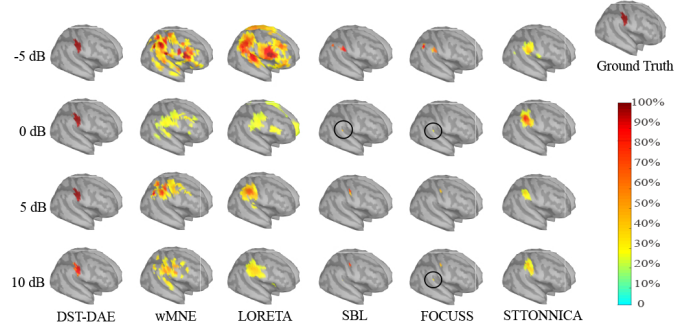


Fig. 5: Source estimates for the single patch source with varying SNRs. Results are presented as the absolute values of the current activities at the peak of the simulated sources and thresholded using Otsu's method. Areas of the sources are all  $5 \text{ cm}^2$ .

### C. Experiment II: Single Patch Source with Varying Spatial Extents

We next assess the performance of DST-DAE for a single patch source with varying spatial extents when the SNR is fixed at  $-5 \text{ dB}$ , which is arguably a challenging scenario for any ESI algorithms to handle. The performance metrics for the compared algorithms are shown in Fig 6. Again, DST-DAE achieves the highest AUC value and the lowest RMSE and DLE values across all the spatial extents. Moreover, despite the low SD value for FOCUSS and SBL when the spatial extent is less than  $6 \text{ cm}^2$ , the performance degrades when the spatial extent increases. However, DST-DAE's SD remains low across all the spatial extents, demonstrating its ability to localize sources precisely with small spatial diffusion.

Fig. 7 provides a source imaging example. The observations align with those in Fig. 5 in that SBL, FOCUSS, wMNE, LORETA, and STTONNICA are unable to accurately estimate the spatial extent due to their biased prior assumptions, but owing to the diversity of the training data, DST-DAE can recover sources with accurate estimation of their locations and spatial extent.

### D. Experiment III: Two Patch Sources with Varying Spatial Patterns

In the third experiment we further evaluate the performance of different algorithms in the case of multiple patch sources. To simplify settings, we consider two patch sources, each with a different ERP time source that is independently generated. In line with the results for the single patch source, DST-DAE yields the best values across AUC, RMSE, and DLE. FOCUSS and SBL achieve slightly lower SD values than DST-DAE for certain source areas (Fig. 8.). However, these two algorithms favor focal sources at the price of sacrificing accuracy for estimating the spatial extents of the patch sources as reflected by their high DLE and RMSE values.

As illustrated in Fig. 9, while the localization accuracy of all the algorithms declines when there are multiple patch sources, DST-DAE provides the best source recovery performance, further demonstrating its superiority over contemporary algorithms in the case of multiple patch sources.

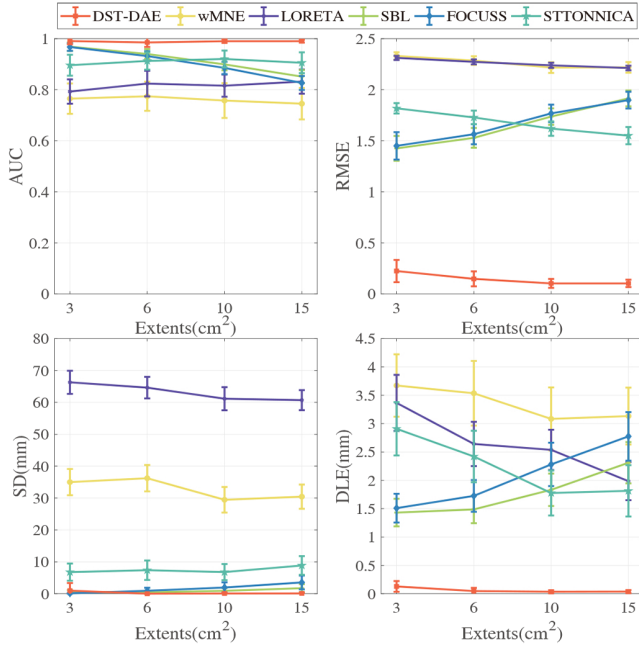


Fig. 6: Performance metrics for the single patch source with varying spatial extents. Results are assessed across 100 Monte Carlo simulations and shown as mean  $\pm$  SEM. SNR is -5 dB.

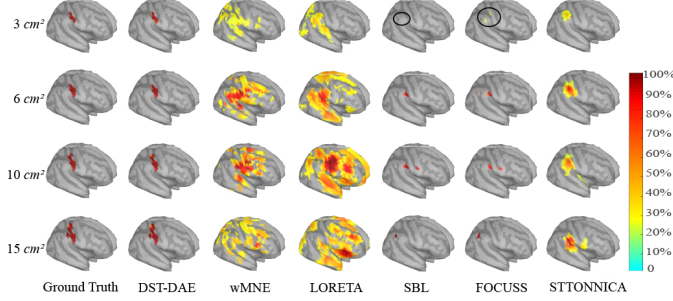


Fig. 7: Source estimates for the single patch source with varying spatial extents. Results are presented as the absolute value of the current activities at the peak and thresholded using Otsu's method.

#### E. Experiment IV: Two Patch Sources with Varying Correlations

Finally, we examine the performance of different algorithms when the activities of the two patch sources are correlated, where the areas of both sources are fixed to  $7 \text{ cm}^2$  and the strength of the correlation is varied from 0 (uncorrelated) to 0.9 (highly-correlated). As shown in Fig. 10, under most settings DST-DAE still dominates the performance metrics that remain stable as the source correlation varies. By contrast, the metrics of other algorithms are more susceptible to the change of the source correlation. In particular, among all the algorithms, STTONNICA shows the most dramatic fluctuations across all the metrics, with the worst performance at  $r = 0.9$ .

To further assess the accuracy of estimating the source temporal dynamics, Fig. 11 shows the time courses of the reconstructed sources by different algorithms. The respective center source from each of the two correlated sources is se-

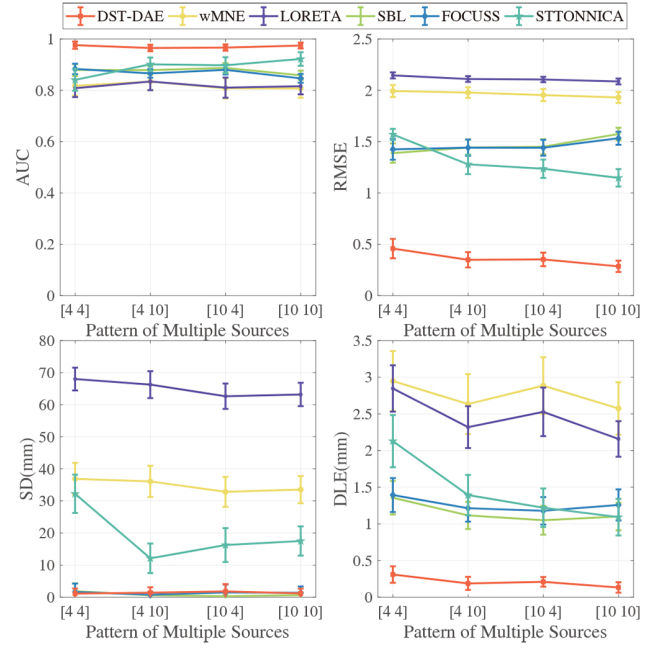


Fig. 8: Performance metrics for two patch sources with varying spatial patterns. The x-axis represents different patterns of the two patch sources, where the numbers indicate the areas of the sources. Results are assessed across 100 Monte Carlo simulations and shown as mean  $\pm$  SEM. SNR is -5 dB.

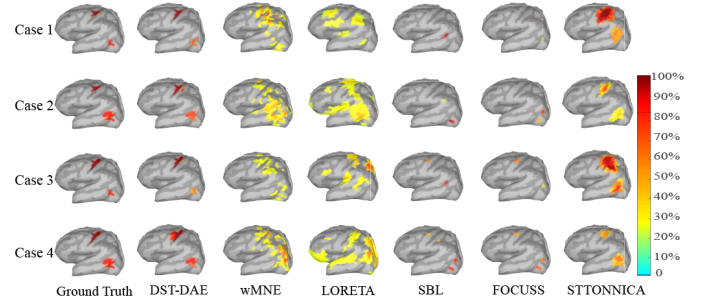


Fig. 9: Source estimates for two patch sources with varying spatial patterns. Results are presented as the absolute value of the current density at the peak and thresholded using Otsu's method.

lected as a reference for the comparison of different methods. Among the compared algorithms, wMNE and LORETA fail to capture the temporal dynamics of the sources entirely. SBL, FOCUSS, and STTONNICA are able to identify the peaks and troughs of one of the sources but not of the other. Note that the reconstructed waveforms by STTONNICA are relatively smooth due to its model assumption regarding the spatio-temporal decomposition that has incorporated temporal constraints. As a consequence of the temporal smoothness of the training data and the powerful learning capability of the denoising autoencoder, DST-DAE can precisely recover temporal dynamics of both sources.



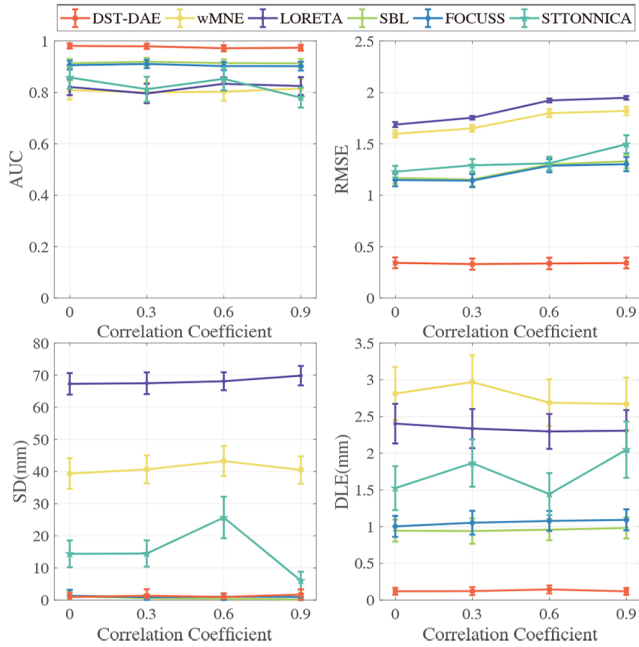


Fig. 10: Performance metrics with varying correlated sources. Results are assessed across 100 Monte Carlo simulations and shown as mean  $\pm$  SEM. SNR is -5 dB. Areas of the sources are all 7  $cm^2$ .

Training Sample	1,500	4,500	9,000	18,000	27,000	36,000
$R^2$	0.253	0.448	0.686	0.856	0.913	0.922

TABLE II:  $R^2$  metric of source signals with varying training sample size.  $R^2$  is measured between the simulated and estimated source signals in the validation set.

#### F. Impact of Training Sample Size

To study the impact of the training sample size on the performance of DST-DAE, we train the neural network with data of different sample sizes under the single patch source condition. We progressively increases the sample size from 1,500 to 36,000, with the batch size of the stochastic gradient descent fixed at 32 and the iteration number during optimization set to 300. As shown in Fig. 12, the training and validation loss functions as well as their gap decrease as the training sample size increases from 1,500 to 27,000 where a plateau is reached, suggesting the gradual improvement of both the representation and generalization performance of the neural network. This observation is corroborated by the trend of the  $R^2$  score shown in Table II, where the increase is small when the training sample size reaches 27,000.

#### G. Real MEG Experiment

Having validated DST-DAE on the simulated data, we further investigate its performance in the analysis of a real MEG data set<sup>2</sup>. The MEG median nerve data of one subject were collected from a stimulation experiment on the left and right thumb, which include 301 and 302 trials, respectively. The

experiment was performed at Massachusetts General Hospital using the Neuromag Vectorview 306 system. There are a total of 306 recording sensors, including 102 MEG magnetometers and 204 MEG planar gradiometers, for which the sampling rate is 1,793 Hz. The length of each trial is 400 ms, including a 100 ms prestimulus baseline. Here we use the 301 left-hand trials for analysis. Moreover, following the suggested data preprocessing settings<sup>3</sup>, we select the 102 magnetometer channels and data within the poststimulus 250 ms time window (starting from 0 ms) as the test signal for DST-DAE. The lead field matrix is calculated based on the subject's individual anatomy via the overlapping spheres model [49].

The TBFs of the MEG data are estimated via SEFA, which represent a total of 80% of the variance of the signal. To reduce the number of training parameters, we ultimately obtain 48 sampling points after antialiasing filtering and downsampling. The cortex space is down-sampled to 1,024 to facilitate the calculation of the convolution kernel. The number of spatial components  $K$  is set to 3. The SNR of the noise block is estimated using prestimulus baseline data. The batch size for SGD is set at 32. The Adam optimizer is selected, in which the learning rate is set to  $10^{-4}$ , hyperparameter  $\beta_1$  is 0.9,  $\beta_2$  is 0.999, and  $\epsilon$  is  $10^{-8}$ . The number of training iterations is set to 300.

Fig. 13 depicts the source imaging results at 35 ms and 85 ms, as previous studies [50] reported that there are substantial brain activities in the contralateral primary somatosensory cortex (cSI) area at 35 ms, and in the cSI area and the secondary somatosensory cortex (SII) area at 85 ms. These prior findings are served as the “ground truth” for comparing different algorithms. As can be observed, the reconstructed sources by wMNE and LORETA are diffuse in which the activation is smeared into the motor area. SBL and FOCUSS yield highly focal sources. However, iSII is not accurately localized by SBL and a spurious source appear in the left ventral temporal cortex for FOCUSS at 85 ms. As for STTONNICA, although it can locate the cSI area at 35 ms as well as cSI and contralateral SII (cSII) at 85 ms, it does not accurately localize the ipsilateral SII (iSII) area at 85 ms but instead yields a few spurious sources in the vicinity of cSI. DST-DAE successfully recovers source activities in the cSI region at 35 ms, and cSI and iSII regions at 85 ms. Interestingly, it is noted that the superior temporal gyrus (STG) region is also activated at 85 ms in the reconstructed source map by DST-DAE. This finding is consistent with the previous source imaging studies [42] where STG rather than cSII is typically activated in the reconstructed maps. This may be explained by the fact that STG and cSII are structurally closely connected.

#### IV. DISCUSSION

In this paper, we propose a novel data-synthesis-based deep learning approach to solve the ESI problem. Compared with LORETA, wMNE, SBL, FOCUSS, and STTONNICA, DST-DAE achieves higher detection sensitivity and smaller error in estimating the source extent and shape in simulation

<sup>2</sup><http://neuroimage.usc.edu/bst/download.php>

<sup>3</sup><https://neuroimage.usc.edu/brainstorm/Tutorials/TutMindNeuromag#Pre-processing>



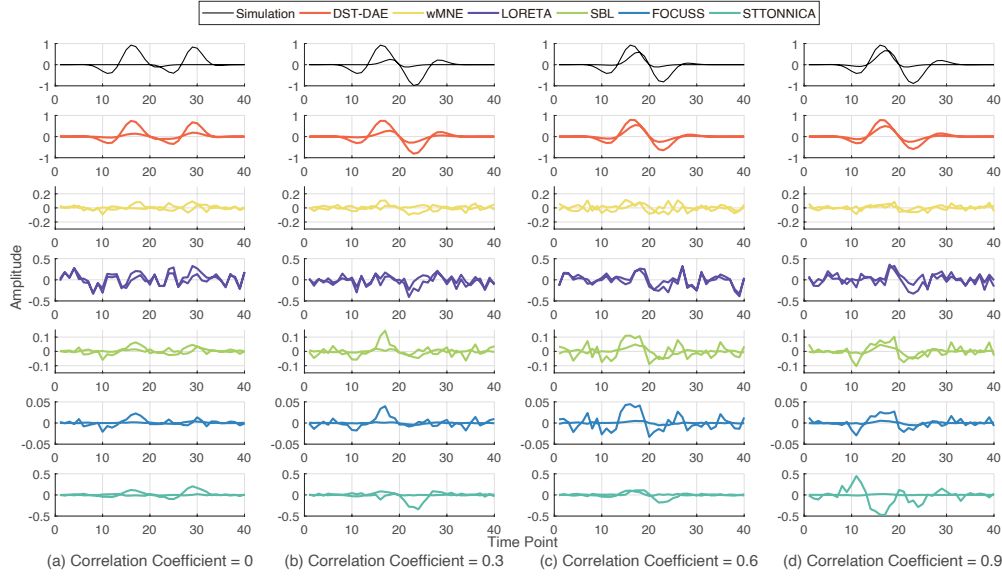


Fig. 11: Reconstruction of time courses with varying correlated sources. The center of each source is selected as a reference for the comparison of different methods. The correlation coefficient between the time courses of the two center sources is varied. Note the range of the y-axis is adapted for each algorithm for visualization purpose. SNR is -5 dB.

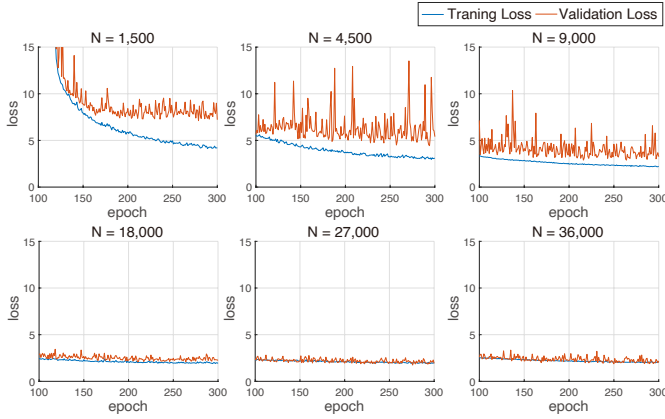


Fig. 12: Training loss and validation loss with varying training sample size. Batch-size of the stochastic gradient descent is set to 32 and the iteration number of optimization to 300.  $N$  is the training sample size.

experiments. In addition, DST-DAE yields more neurophysiologically plausible source estimation on a realistic MEG dataset. The superiority of our method is owing to how the prior information is leveraged in the algorithm. Specifically, a notable difference between DST-DAE and traditional ESI methods is that the prior information regarding source signals is not enforced via mathematical constraints but rather the data synthesis strategy that generates a variety of states from the spatial-temporal prior space, which further guarantees the generalizability of the neural network and the validity of the simulated data. Previous studies suggested that brain activities tend to be spatially contiguous and locally homogeneous [38]–[40]. Our method exploits these spatial properties to generate spatial states, which enables the network to yield

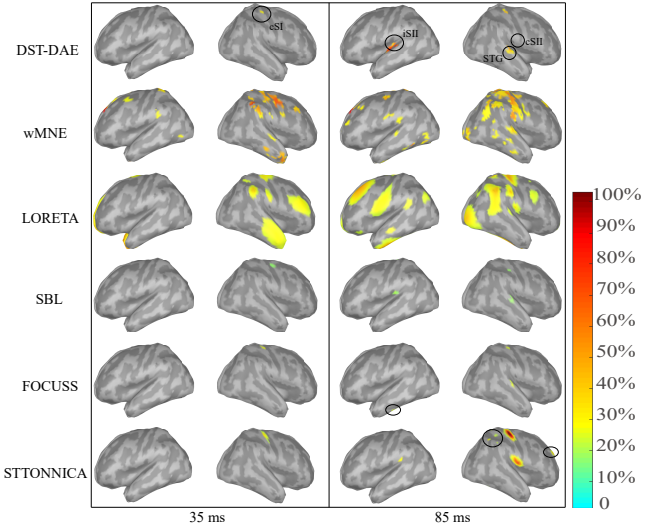


Fig. 13: Comparison of source imaging of MEG data at 35 and 85 ms. The MEG median nerve data was collected in a stimulation experiment on the thumbs. The contralateral primary somatosensory cortex (cSI) area, the secondary somatosensory cortices (SII) area, and the superior temporal gyrus (STG) area are circled in the first row.

estimates with compact and accurate extents. Unlike traditional methods [51], [52] where TBFs are directly utilized as the temporal components of source signals under probabilistic graphic models, our method instead uses TBFs as the basis to generate the temporal components of the source signals, which is more likely able to capture the diverse dynamics of brain activities. Moreover, DST-DAE can robustly extract spatio-temporal features from highly noisy E/MEG signals due to the intrinsic denoising capability of the DAE. The latent-

space representation provided by the DAE allows DST-DAE to extract high-level features from noisy E/MEG signals, which effectively regularizes the solution obtained from discriminative learning.

#### A. Hyperparameter Tuning

In the proposed model, key hyperparameters are the kernel size, the stride (step size), and the number of feature maps. Here we assess the impact of these hyperparameters on the predictive performance of the model. We first generate a training set and a validation set with equal sample size ( $N = 13,500$  trials) using our data synthesis approach. Each trial of 64-channel synthetic signals contains 40 time points and is corrupted by an additive noise with an SNR of -5 dB. The source space consists of 1,024 vertices. Subsequently, we train multiple models by varying the hyperparameters using the training set, where the training batch size is 32 and the number of epochs is 250. The predictive performance of the trained models is then compared on the validation set. Since hyperparameter search is time-consuming, we only search within a confined set of hyperparameter values in order to save computational cost. Moreover, each time we only vary one hyperparameter with respect to a base model. The kernel size of the base model is  $1 \times 3$ ,  $1 \times 4$ ,  $8 \times 1$ , and  $10 \times 1$ , for the temporal encoding blocks, temporal decoding blocks, spatial encoding blocks, and spatial decoding blocks, respectively. These kernel sizes are smaller than the ones in Section II for the purpose of reducing the computational cost. The stride is  $1 \times 2$  and  $2 \times 1$  for the temporal and spatial blocks, respectively. Finally, to account for potential variance of the data, we repeat the above procedure for 5 runs and calculated the average  $R^2$  between the predicted source signals and the true source signals.

1) *Kernel Size*: The kernel size determines the receptive field of the neural network and hence influences the modeling capability – the larger the kernel size is, the more global features the neural network is able to capture. However, the model complexity will also increase with the expansion of the parameter space.

Table III shows the predictive performance of the neural network by varying the kernel size, where each column corresponds to varying the kernel size of one block while fixing the other hyperparameters in the base model. For the temporal blocks, a temporal encoder kernel of  $1 \times 5$  and a temporal decoder kernel of  $1 \times 6$  lead to the highest  $R^2$  score in the validation set. Moreover, the difference of the predictive performance between the training set and the validation set is smaller than those associated with other kernel sizes. For the spatial decoder, the optimal kernel size is  $20 \times 1$ . Notably, the predictive performance declines dramatically when the kernel size increases to 8. In terms of the spatial encoder, a kernel size equal to the channel number achieves the best predictive performance, which is in line with the EEG decoding results reported in [32].

2) *Step Size*: The step size (i.e., stride) of the kernel refers to the rate of downsampling in the decoder layers and upsampling in the encoder layers, which determines the scale

of the local information each feature map can capture and affects the number of the neural network layers. For instance, an input with 40 dimensions needs 3 layers with the stride of 2 to be reduced to an output with  $40/2^3 = 5$  dimensions. We separately test three different strides, namely 2, 4, and 8, for the temporal encoder and decoder and the spatial decoder. As shown in Table IV, the predictive performance of the neural network deteriorates as the step size of the temporal encoder/ decoder increases. Notably, a drastic decrease of the performance occurs when the step size is 8 since a step size significantly larger than the kernel size may lead to adverse effects on training the neural network. Besides, the overfitting issue aggravates as the step size of the spatial decoder increases.

3) *Feature Map*: We compare three modes for the number of feature maps: 1) the number of feature maps increases for the encoder and decreases for the decoder by 2-fold between adjacent layers; 2) the number of feature maps is fixed to 32 for the encoder while decreases by 2-fold between adjacent decoder layers; and 3) the number of feature maps decreases for both the encoder and decoder by 2-fold between adjacent layers. As shown in Table IV, the first mode attains the best predictive performance, arguing for an hourglass-shaped structure for the proposed neural network.

#### B. Time Complexity

For the real MEG dataset, the total number of trainable parameters is 509,846, the batch size of the stochastic gradient descent is 32, and the number of training iterations is 300. With the network architecture and hyperparameters fixed, the time complexity depends on the number of training samples, which is  $\mathcal{O}(n)$ . The mean run-times per epoch for different training sample sizes on a single 12 GB TITAN-Xp GPU are shown in Table V. Furthermore, to measure the time it takes to make predictions using the trained neural network, we made 100 predictions on the real MEG data that contains 48 sampling points across 102 channels. The average prediction runtime for each dataset is  $3.598 \pm 0.152$  sec.

In DST-DAE, although the training process is time-consuming, once trained the model can be applied to new data to make predictions without the need of optimization as traditional methods do.

#### C. Limitations and Future Directions

Reconstructing a high-resolution source space entails the estimation of a large number of parameters and hyperparameters prohibitive to the available computing resource. In order to ease the computational burden, we reduce the dimensionality of the parameter space by sampling the source space at a relatively low spatial resolution. This limitation is expected to become less problematic with the rapid growth in computing power.

In this paper, we have focused on assessing the predictive performance of DST-DAE for single patch and two patch sources, where the number of the patch source is assumed to be known in generating the training data. It remains to be tested whether the predictive performance persists when

TABLE III:  $R^2$  scores for source reconstruction with varying kernel sizes. Each column shows the performance of neural network with only the kernel size in the respective layer changed.

$R^2$ Score	Kernel Size Settings											
	Temporal En/Decoder				Spatial Decoder				Spatial Encoder			
	1×3/4	1×5/6	1×7/8	1×9/10	20×1	10×1	6×1	3×1	64×1	32×1	16×1	8×1
Training Set	0.738	0.734	0.726	0.697	0.768	0.736	0.711	0.678	0.774	0.756	0.749	0.735
Validation Set	0.717	0.721	0.701	0.681	0.697	0.715	0.689	0.650	0.732	0.729	0.723	0.714
Total Parameters	312,250	335,226	358,202	381,178	394,170	312,250	279,482	254,906	417,978	451,130	377,786	312,250

TABLE IV:  $R^2$  scores for source reconstruction with varying hyperparameter settings. Each column shows the performance of neural network with only the hyperparameter in the respective layer changed. TE, TD, and SD represent the temporal encoder, temporal decoder, and the spatial decoder, respectively. “inc” and “dec” stand for “increase” and “decrease”, respectively.

$R^2$ Score	Hyperparameter Settings											
	Step Size (TE)			Step Size (TD)			Step Size (SD)			Feature Map (Encoder)		
	2	4	8	2	4	8	2	4	8	2x inc	constant	2x dec
Training Set	0.737	0.733	0.620	0.736	0.725	0.488	0.738	0.747	0.757	0.736	0.716	0.719
Validation Set	0.720	0.706	0.585	0.718	0.716	0.467	0.719	0.714	0.712	0.718	0.683	0.689
Total Parameters	312,250	305,146	300,586	312,250	307,066	300,242	312,250	281,242	270,906	312,250	155,970	330,130

Training sample size	1,500	4,500	9,000	18,000	27,000	36,000
Time/epoch (s)	9.2	28.8	61.2	125.2	170.2	232.4

TABLE V: Mean runtimes per epoch for different training sample sizes on a single 12 GB TITAN-Xp GPU. The number of training iterations is 300.

the number of patch sources exceeds two. Since more source configurations may lead to highly similar E/MEG patterns in the case of multiple patch sources, a potential challenge will be designing an appropriate loss function sensitive to the subtle difference between these source configurations. Moreover, to the best of our knowledge, current deep learning-based ESI methods restrict the possible numbers of patch sources in a single training set, as mixing different numbers of patch sources in the training set may lead to a decrease of the reconstruction performance. Therefore, our future work will focus on the design of better architectures and loss functions for dealing with multisources.

## V. CONCLUSION

In conclusion, we have proposed a novel neural network method termed DST-DAE to solve the ESI problem. Compared with traditional methods that rely on optimization constraints to estimate sources, DST-DAE generate large-scale training sets via a data synthesis strategy, allowing the neural network to automatically learn the sensor-to-source mapping. By leveraging prior knowledge regarding the spatio-temporal characteristics of brain activities during data generation, prior information can be readily incorporated without the need of sophisticated mathematical modeling and can conveniently be applied to new data without further optimization. Furthermore, the neural network integrates discriminative learning and latent-space representation under the framework of the DAE, where the latent-space representation in the DAE designed

with specific blocks is able to extract a robust spatio-temporal feature from highly noisy E/MEG signals, effectively regularizing the solution obtained from discriminative learning. Both simulation and realistic data analyses demonstrate that DST-DAE outperforms traditional ESI approaches in a range of source settings. Therefore, the method provides a useful tool for source localization in both basic science and translational studies.

## REFERENCES

- [1] B. He, L. Yang, C. Wilke, and H. Yuan, “Electrophysiological imaging of brain activity and connectivity—challenges and opportunities,” *IEEE Transactions on Biomedical Engineering*, vol. 58, no. 7, pp. 1918–1931, Jul. 2011.
- [2] C. M. Michel, M. M. Murray, G. Lantz, S. Gonzalez, L. Spinelli, and R. G. de Peralta, “EEG source imaging,” *Clinical Neurophysiology*, vol. 115, no. 10, pp. 2195–2222, Oct. 2004.
- [3] S. Baillet, J. Mosher, and R. Leahy, “Electromagnetic brain mapping,” *IEEE Signal Processing Magazine*, vol. 18, no. 6, pp. 14–30, 2001.
- [4] M. S. Hämäläinen and R. J. Ilmoniemi, “Interpreting magnetic fields of the brain: minimum norm estimates,” *Medical & Biological Engineering & Computing*, vol. 32, no. 1, pp. 35–42, Jan. 1994.
- [5] A. M. Dale and M. I. Sereno, “Improved localization of cortical activity by combining EEG and MEG with MRI cortical surface reconstruction: A linear approach,” *Journal of Cognitive Neuroscience*, vol. 5, no. 2, pp. 162–176, Apr. 1993.
- [6] R. Pascual-Marqui, C. Michel, and D. Lehmann, “Low resolution electromagnetic tomography: a new method for localizing electrical activity in the brain,” *International Journal of Psychophysiology*, vol. 18, no. 1, pp. 49–65, Oct. 1994.
- [7] R. Grech, T. Cassar, J. Muscat, K. P. Camilleri, S. G. Fabri, M. Zervakis, P. Xanthopoulos, V. Sakkalis, and B. Vanrumste, “Review on solving the inverse problem in EEG source analysis,” *Journal of NeuroEngineering and Rehabilitation*, vol. 5, no. 1, p. 25, 2008.
- [8] H. Becker, L. Albera, P. Comon, R. Gribonval, F. Wendling, and I. Merlet, “Brain-source imaging: From sparse to tensor models,” *IEEE Signal Processing Magazine*, vol. 32, no. 6, pp. 100–112, Nov. 2015.
- [9] I. F. Gorodnitsky, J. S. George, and B. D. Rao, “Neuromagnetic source imaging with FOCUSS: a recursive weighted minimum norm algorithm,” *Electroencephalography and Clinical Neurophysiology*, vol. 95, no. 4, pp. 231–251, Oct. 1995.
- [10] L. Ding and B. He, “Sparse source imaging in electroencephalography with accurate field modeling,” *Human brain mapping*, vol. 29, no. 9, pp. 1053–1067, 2008.

- [11] P. Xu, Y. Tian, H. Chen, and D. Yao, "Lp norm iterative sparse solution for eeg source localization," *IEEE transactions on biomedical engineering*, vol. 54, no. 3, pp. 400–409, 2007.
- [12] D. Wipf and S. Nagarajan, "A unified bayesian framework for MEG/EEG source imaging," *NeuroImage*, vol. 44, no. 3, pp. 947–966, Feb. 2009.
- [13] J. P. Owen, D. P. Wipf, H. T. Attias, K. Sekihara, and S. S. Nagarajan, "Performance evaluation of the champagne source reconstruction algorithm on simulated and real m/eeg data," *Neuroimage*, vol. 60, no. 1, pp. 305–323, 2012.
- [14] W. Wu, S. Nagarajan, and Z. Chen, "Bayesian machine learning: Eeg/meg signal processing measurements," *IEEE Signal Processing Magazine*, vol. 33, no. 1, pp. 14–36, 2015.
- [15] D. P. Wipf, J. P. Owen, H. T. Attias, K. Sekihara, and S. S. Nagarajan, "Robust bayesian estimation of the location, orientation, and time course of multiple correlated neural sources using MEG," *NeuroImage*, vol. 49, no. 1, pp. 641–655, Jan. 2010.
- [16] C. Cai, M. Diwakar, A. Hashemi, S. Haufe, K. Sekihara, and S. S. Nagarajan, "Robust estimation of noise for electromagnetic brain imaging with the champagne algorithm," *NeuroImage*, p. 117411, 2020.
- [17] K. Liu, Z. L. Yu, W. Wu, Z. Gu, and Y. Li, "Straps: A fully data-driven spatio-temporally regularized algorithm for m/eeg patch source imaging," *International journal of neural systems*, vol. 25, no. 04, p. 1550016, 2015.
- [18] P. A. Valdés-Sosa, M. Vega-Hernández, J. M. Sánchez-Bornot, E. Martínez-Montes, and M. A. Bobes, "EEG source imaging with spatio-temporal tomographic nonnegative independent component analysis," *Human Brain Mapping*, vol. 30, no. 6, pp. 1898–1910, Jun. 2009.
- [19] F. G. Awan, O. Saleem, and A. Kiran, "Recent trends and advances in solving the inverse problem for EEG source localization," *Inverse Problems in Science and Engineering*, vol. 27, no. 11, pp. 1521–1536, Jul. 2018.
- [20] T. R. Knösche, M. Gräser, and A. Anwander, "Prior knowledge on cortex organization in the reconstruction of source current densities from EEG," *NeuroImage*, vol. 67, pp. 7–24, Feb. 2013.
- [21] A. M. Dale, A. K. Liu, B. R. Fischl, R. L. Buckner, J. W. Belliveau, J. D. Lewine, and E. Halgren, "Dynamic statistical parametric mapping," *Neuron*, vol. 26, no. 1, pp. 55–67, Apr. 2000.
- [22] S. Arridge, P. Maass, O. Öktem, and C.-B. Schönlieb, "Solving inverse problems using data-driven models," *Acta Numerica*, vol. 28, pp. 1–174, 2019.
- [23] U. R. Abeyratne, Y. Kinouchi, H. Oki, J. Okada, F. Shichijo, and K. Matsumoto, "Artificial neural networks for source localization in the human brain," *Brain Topography*, vol. 4, no. 1, pp. 3–21, 1991.
- [24] G. Van Hoey, J. De Clercq, B. Vanrumste, R. Van de Walle, I. Lemahieu, M. D'Havé, and P. Boon, "Eeg dipole source localization using artificial neural networks," *Physics in Medicine & Biology*, vol. 45, no. 4, p. 997, 2000.
- [25] M. Yuasa, Q. Zhang, H. Nagashino, and Y. Kinouchi, "Eeg source localization for two dipoles by neural networks," in *Proceedings of the 20th Annual International Conference of the IEEE Engineering in Medicine and Biology Society. Vol. 20 Biomedical Engineering Towards the Year 2000 and Beyond (Cat. No. 98CH36286)*, vol. 4. IEEE, 1998, pp. 2190–2192.
- [26] U. R. Abeyratne, G. Zhang, and P. Saratchandran, "Eeg source localization: a comparative study of classical and neural network methods," *International journal of neural systems*, vol. 11, no. 04, pp. 349–359, 2001.
- [27] I. Goodfellow, Y. Bengio, and A. Courville, *Deep learning*. MIT press, 2016.
- [28] R. Sun, A. Sohrabpour, S. Ye, and B. He, "Sifnet: Electromagnetic source imaging framework using deep neural networks," *bioRxiv*, 2020.
- [29] P. Vincent, H. Larochelle, I. Lajoie, Y. Bengio, P.-A. Manzagol, and L. Bottou, "Stacked denoising autoencoders: Learning useful representations in a deep network with a local denoising criterion," *Journal of machine learning research*, vol. 11, no. 12, 2010.
- [30] B. He, T. Musha, Y. Okamoto, S. Homma, Y. Nakajima, and T. Sato, "Electric dipole tracing in the brain by means of the boundary element method and its accuracy," *IEEE Transactions on Biomedical Engineering*, vol. BME-34, no. 6, pp. 406–414, Jun. 1987.
- [31] M. Hamalainen and J. Sarvas, "Realistic conductivity geometry model of the human head for interpretation of neuromagnetic data," *IEEE Transactions on Biomedical Engineering*, vol. 36, no. 2, pp. 165–171, Feb. 1989.
- [32] R. T. Schirrmester, J. T. Springenberg, L. D. J. Fiederer, M. Glasstetter, K. Eggersperger, M. Tangermann, F. Hutter, W. Burgard, and T. Ball, "Deep learning with convolutional neural networks for brain mapping and decoding of movement-related information from the human eeg. arxiv, 2017," *arXiv preprint arXiv:1703.05051*.
- [33] S. Sakhavi, C. Guan, and S. Yan, "Learning temporal information for brain-computer interface using convolutional neural networks," *IEEE Transactions on Neural Networks and Learning Systems*, vol. 29, no. 11, pp. 5619–5629, 2018.
- [34] O. Kwon, M. Lee, C. Guan, and S. Lee, "Subject-independent brain-computer interfaces based on deep convolutional neural networks," *IEEE Transactions on Neural Networks and Learning Systems*, pp. 1–14, 2019.
- [35] A. Odena, V. Dumoulin, and C. Olah, "Deconvolution and checkerboard artifacts," *Distill*, vol. 1, no. 10, p. e3, 2016.
- [36] D.-A. Clevert, T. Unterthiner, and S. Hochreiter, "Fast and accurate deep network learning by exponential linear units (elus)," *arXiv preprint arXiv:1511.07289*, 2015.
- [37] S. Ioffe and C. Szegedy, "Batch normalization: Accelerating deep network training by reducing internal covariate shift," *arXiv preprint arXiv:1502.03167*, 2015.
- [38] J. X. Tao, A. Ray, S. Hawes-Ebersole, and J. S. Ebersole, "Intracranial eeg substrates of scalp eeg interictal spikes," *Epilepsia*, vol. 46, no. 5, pp. 669–676, 2005.
- [39] M. Hämäläinen, R. Hari, R. J. Ilmoniemi, J. Knuutila, and O. V. Lounasmaa, "Magnetoencephalography—theory, instrumentation, and applications to noninvasive studies of the working human brain," *Reviews of modern Physics*, vol. 65, no. 2, p. 413, 1993.
- [40] A. Destexhe, D. Contreras, and M. Steriade, "Spatiotemporal analysis of local field potentials and unit discharges in cat cerebral cortex during natural wake and sleep states," *Journal of Neuroscience*, vol. 19, no. 11, pp. 4595–4608, 1999.
- [41] S. S. Nagarajan, H. T. Attias, K. E. Hild, and K. Sekihara, "A probabilistic algorithm for robust interference suppression in bioelectromagnetic sensor data," *Statistics in medicine*, vol. 26, no. 21, pp. 3886–3910, 2007.
- [42] W. Ou, M. S. Hämäläinen, and P. Golland, "A distributed spatio-temporal eeg/meg inverse solver," *NeuroImage*, vol. 44, no. 3, pp. 932–946, 2009.
- [43] A. Gramfort, T. Papadopoulos, E. Olivi, and M. Clerc, "Openmeeeg: opensource software for quasistatic bioelectromagnetics," *Biomedical engineering online*, vol. 9, no. 1, p. 45, 2010.
- [44] F. Tadel, S. Baillet, J. C. Mosher, D. Pantazis, and R. M. Leahy, "Brainstorm: a user-friendly application for meg/eeg analysis," *Computational intelligence and neuroscience*, vol. 2011, 2011.
- [45] D. P. Kingma and J. Ba, "Adam: A method for stochastic optimization," *arXiv preprint arXiv:1412.6980*, 2014.
- [46] A. Gotmare, N. S. Keskar, C. Xiong, and R. Socher, "A closer look at deep learning heuristics: Learning rate restarts, warmup and distillation," *arXiv preprint arXiv:1810.13243*, 2018.
- [47] D. L. Alexander, A. Tropsha, and D. A. Winkler, "Beware of r<sup>2</sup>: simple, unambiguous assessment of the prediction accuracy of qsar and qspr models," *Journal of chemical information and modeling*, vol. 55, no. 7, pp. 1316–1322, 2015.
- [48] N. Otsu, "A threshold selection method from gray-level histograms," *IEEE transactions on systems, man, and cybernetics*, vol. 9, no. 1, pp. 62–66, 1979.
- [49] M. Huang, J. C. Mosher, and R. Leahy, "A sensor-weighted overlapping-sphere head model and exhaustive head model comparison for meg," *Physics in Medicine & Biology*, vol. 44, no. 2, p. 423, 1999.
- [50] R. Hari and N. Forss, "Magnetoencephalography in the study of human somatosensory cortical processing," *Philosophical Transactions of the Royal Society of London. Series B: Biological Sciences*, vol. 354, no. 1387, pp. 1145–1154, 1999.
- [51] J. M. Zumer, H. T. Attias, K. Sekihara, and S. S. Nagarajan, "Probabilistic algorithms for meg/eeg source reconstruction using temporal basis functions learned from data," *NeuroImage*, vol. 41, no. 3, pp. 924–940, 2008.
- [52] N. J. Trujillo-Barreto, E. Aubert-Vázquez, and W. D. Penny, "Bayesian m/eeg source reconstruction with spatio-temporal priors," *Neuroimage*, vol. 39, no. 1, pp. 318–335, 2008.